

This item is the archived peer-reviewed author-version of:

Digital stroboscopic holography setup for deformation measurement at both quasi-static and acoustic frequencies

Reference:

De Greef Daniël, Soons Joris, Dirckx Joris.- Digital stroboscopic holography setup for deformation measurement at both quasi-static and acoustic frequencies

International Journal of Optomechatronics - ISSN 1559-9612 - 8:4(2014), p. 275-291

Full text (Publishers DOI): <http://dx.doi.org/doi:10.1080/15599612.2014.942928>

Handle: <http://hdl.handle.net/10067/1200730151162165141>

Digital stroboscopic holography setup for deformation measurement at both quasi-static and acoustic frequencies

Daniël De Greef^a, Joris Soons^a, Joris J. J. Dirckx^a

^a Laboratory of Biomedical Physics, University of Antwerp, Groenenborgerlaan 171, 2020 Antwerp, Belgium

Abstract

A setup for digital stroboscopic holography that combines the advantages of full-field digital holographic interferometry with a high temporal resolution is presented. The setup can be used to identify and visualize complicated vibrational patterns with nanometer amplitudes, ranging from quasi-static to high frequency vibrations. By using a high-energy pulsed laser, single-shot holograms can be recorded and stability issues are avoided. Results are presented for an acoustically stimulated rubber membrane and the technique is evaluated by means of an accuracy and a repeatability test. The presented technique offers wide application possibilities in areas such as biomechanics and industrial testing.

1. Introduction

In the past, numerous holographic techniques have been developed and applied to measure full-field vibrational motion of a surface in various frequency ranges. Time-average holography has been widely used, in analogue as well as digital version (Powell and Stetson 1965; Rosowski et al. 2009). It requires a technically simpler setup than the technique presented in this work in terms of controlling electronics, yet still provides very valuable data for a lot of applications, as it supplies quantitative information regarding harmonic deformations, changing refractive indices etc. Various setups for digital double-exposure stroboscopic holography have been published as well (Hariharan and Oreb 1986; Hernandez-Montes et al. 2009; Furlong et al. 2009). In recent years, a new concept of stroboscopic holography has been implemented, based on multiple very short phase-locked pulses cycling through the vibration period so that the entire time-dependent motion of the studied surface can be visualized (Pedrini, Osten, and Gusev 2006; Trillo et al. 2009; Cheng et al. 2010; De Greef and Dirckx 2012; De Greef and Dirckx 2014).

The setup for stroboscopic holography that is presented in this paper allows imaging of dynamic out-of-plane displacements over the entire surface of an object as a function of time over a very wide frequency range. The current setup has advantages over earlier published methods (Pedrini, Osten, and Gusev 2006; Trillo et al. 2009). A wider frequency range (measured and presented: 5 Hz – 16.7 kHz; theoretically: 0 Hz – 250

kHz), a shorter acquisition time and a better spatial resolution than in similar setups can be achieved, as will be covered in detail in the discussion of this paper. Since both amplitude and phase of the excitation signal are precisely measured relative to the ultra-short high-energy laser pulses, the complex transfer function (i.e. magnitude and phase) of the studied surface relative to the input is available after the experiment. The setup is controlled and monitored using two function generators, an oscilloscope, a PC and custom made electronics containing a programmed microprocessor. Results from measurements on a test subject will be presented and discussed, as well as results from two independent quality tests for the setup. The current setup is optimized and being used for the study of eardrum vibrations of humans, other mammals and avian species.

2. Method

2.1 Concept

2.1.1 Digital holography

In digital holography, the interference pattern of a mutually coherent object beam and reference beam is recorded on a digital imaging matrix, such as a CCD or a CMOS. The main advantage over analogue holography, aside from flexibility and off-line reconstruction, is the direct access to the optical phase of the object wave after digital reconstruction. Therefore, quantitative information about the object's displacement between two recorded states is acquired by simply subtracting the reconstructed object wave phase maps of the two holograms. The result is a wrapped phase difference map. The same result can be obtained by a complex division of the reconstructed holograms, but this did not yield different results from the subtraction method described before.

By applying a two-dimensional phase-unwrapping algorithm (Herráez et al. 2002), the actual phase difference $\Delta\phi$ between the two object waves is obtained. The change in optical path length $\Delta\delta$ of the object beam between the two recorded states is related to the change in object wave phase $\Delta\phi$ through $\Delta\delta = \lambda \frac{\Delta\phi}{2\pi}$, with λ the optical wavelength. In our setup, the illumination direction is parallel to the observation direction, so that the object's deformation d is related to the change in optical path length through $d = \frac{\Delta\delta}{2}$, so that:

$$d = \lambda \frac{\Delta\phi}{4\pi}. \quad (1)$$

Using this equation for all object points, the full field displacement map of the deformation can be calculated.

All calculations in this paper, as well as experiment control, are performed in Matlab (The Mathworks). In order to minimize the needed calculation time, a region of interest (ROI) is determined by the user along the border of the object and the unwrapping algorithm is only applied to this ROI, which drastically reduces the computational load. In order to have a spatial displacement reference, the inclusion of several decades of object points (pixels) with a known displacement equal or close enough to zero in the ROI is essential.

Reconstruction of a digital hologram starts by multiplication of the recorded interference pattern with the numerical equivalent of the reference wave. The resulting wave is then propagated numerically over the distance d between the CCD and the object that was used during the recording. For this purpose we use the Fresnel diffraction formula. The Fresnel approximation, required for this approach, is allowed as the condition for it reads (derived from Kreis 2005):

$$F := \left(\frac{D_{\text{CCD}} + D_{\text{obj}}}{d} \right)^2 \ll 1, \quad (2)$$

with D_{CCD} and D_{obj} the lateral dimensions of the CCD-targeted and the object, respectively, and d the distance between CCD and object. In our setup, these values are $D_{\text{CCD}} = 8.5$ mm, $D_{\text{obj}} = 8$ mm, $d = 160$ mm, resulting in $F = 0.011$.

The total reconstruction formula for calculating the reconstructed hologram b is as follows (Kreis 2005):

$$b(n\Delta x, m\Delta y) = e^{i\pi d\lambda \left(\frac{n^2}{N^2\Delta\xi^2} + \frac{m^2}{M^2\Delta\eta^2} \right)} \sum_{k=0}^{N-1} \sum_{l=0}^{M-1} h(k, l) r^*(k, l) e^{\frac{i\pi}{d\lambda} (k^2\Delta\xi^2 + l^2\Delta\eta^2)} e^{-2i\pi \left(\frac{kn}{N} + \frac{lm}{M} \right)}, \quad (3)$$

with n, m the image indices; $\Delta x, \Delta y$ the image pixel center-to-center distances; $\Delta\xi, \Delta\eta$ the CCD pixel distances; λ the optical wavelength of the laser; N, M the number of pixels in x - and y -direction; k, l the CCD indices; h the recorded hologram and r^* the conjugated reference wave. The advantage of this technique over phase-shifting methods (Yamaguchi and Zhang 1997) is that a single hologram is sufficient to extract both wave intensity and phase. The drawback is that there will be other orders of diffraction visible on the image (the DC term and the conjugated twin image), so that not all pixels can be used to display the real image.

2.1.2 Stroboscopic digital holography

In stroboscopic digital holography, a periodically moving object is illuminated by either one or multiple very short pulses, synchronized to a single phase within the motion period. After combining this vibration hologram with a hologram of the object at rest state, a full field displacement map of the objects displacement at the chosen vibration phase is obtained. By cycling the phase-locked illumination pulse stepwise through the vibration period (figure 1) one can collect displacement maps for evenly distributed time instants within the period. Therefore, we are able to measure the object's full-field deformation as a function of time with a temporal resolution that is only limited by the pulse length of the laser and the precision of the triggering. Obviously, the imaged object has to fulfill generic requirements for digital holography such as short-term nanometer stability, sufficient reflectivity and dimensions that do not cause the interference pattern to violate the Nyquist-Shannon sampling theorem for the chosen viewing distance.

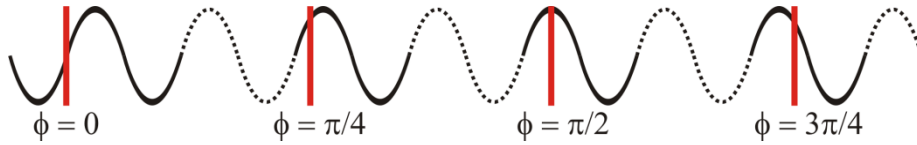


Figure 1: The concept of stroboscopically illuminated holography. Very short illumination pulses are phase-locked and cycle stepwise through the vibration period.

2.2 Setup

2.2.1 Optical arrangement

An overview of the setup, including optical, electronic and acoustic components, is depicted in figure 2. The used laser is a frequency doubled pulsed Nd:YAG laser (JK Lasers, $\lambda = 532$ nm), producing pulses of up to 5 mJ with a duration of 8 ns. Its beam is broadened by a Galilean beam expander (GBE) and polarization is controlled using a $\lambda/2$ plate, before it is divided into an object and reference beam (OB and RB) by a polarizing beam splitter (PBS). The OB is partially reflected by a non-polarizing beam splitter (NPBS 1), directing it towards the object. This NPBS allows a perpendicular illumination of the object and therefore maximizes the resolution of out-of-plane displacement. The OB is reflected and diffracted by the object and travels back through the NPBS 1 towards NPBS 2, where it is combined with the RB. Both waves pass a polarizer in front of the CCD that is aligned with the polarization of the RB, so that only the OB light of the same polarization hits the target, thus maximizing interference fringe contrast. Indeed, when the used object surface is diffuse, the scattered light will be randomly polarized so that only the relevant half of the object light passes the polarizer and interferes with the RB. In our applications, specular reflecting surfaces are avoided, but if it is unavoidable, an additional $\lambda/2$ plate should be placed in the OB to realign the polarization of both waves. The OB and RB interference pattern is recorded by a CCD camera (AVT Pike 505-B, 2452x2054, 14bit). The frame rate of the camera at the highest resolution is 6.5 fps. Often, lower resolution is sufficient and frame rate can be increased to 10 fps, but not higher as the pulsed laser cannot produce high-energy pulses at frequencies > 10 Hz.

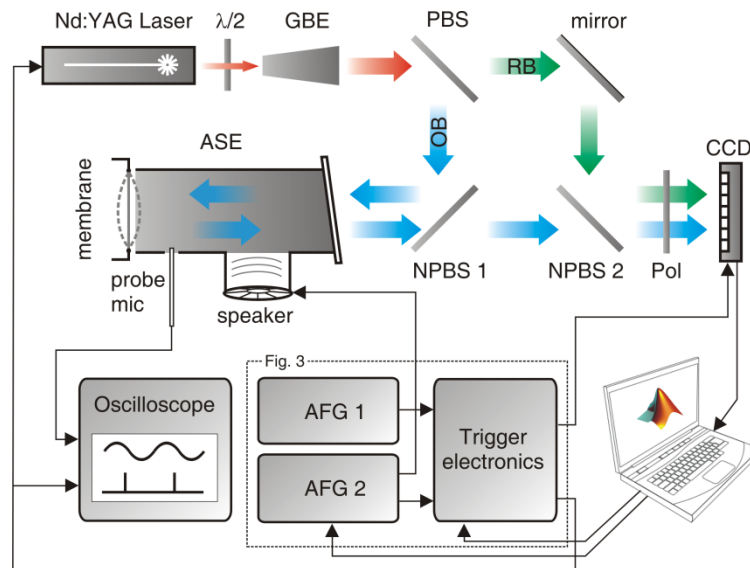


Figure 2: Schematic overview of the setup. Components are discussed in Section 2.2. GBE: Galilean beam expander. (N)PBS: (Non-) polarizing beam splitter. OB: object beam. RB: Reference beam. ASE: Acoustic stimulation element. Pol: Polarizer. CCD: Charge-coupled device. AFG: Arbitrary function generator.

2.2.2 Electronic aspects: trigger sequence

All electronic components are controlled and/or monitored by one or more of the following: a personal computer, two function generators (Tektronix AFG 3102), an oscilloscope (Tektronix TDS 210) and a piece of custom made trigger electronics, containing a microprocessor (Microchip PIC18F2410). A close-up view of the trigger timing sequence is shown in Figure 3. The first generator provides pulses to the microchip with the same frequency as the camera frame rate. The second generator produces the excitation stimulus signal and a series of pulses synchronized to the stimulus that serves as the second input for the microprocessor.

The program on the chip selects the first pulse of the AFG 2 in every active interval of AFG 1. In 'freerun mode', this series of pulses is passed to the laser without further alteration. In this way, the laser is flashing at a fixed rate, allowing the laser cavity temperature to stabilize. To record the rest frame, the stimulus is disabled, the 'freerun mode' is applied and the camera is triggered manually. After this, the stimulus signal is enabled and a USB-signal from the PC initiates a series of delays upon the laser trigger pulses that is programmed in the microchip. This program delays every outgoing pulse with an ascending multiple integer of $\delta = P/n$, where P is the vibration period and n is the number of desired frames within a period. At the same time, the program ensures that one hardware trigger pulse is sent to the camera for every delayed pulse. For every pulse, the delay time is increased by δ , so that holograms are recorded stepwise through the entire vibration period. This will be repeated until n frames are delayed, the last frame being delayed by exactly P , after which the program ends, the camera trigger pulses will be stopped and the microchip will re-enter the 'freerun' mode.

Although the frequency of laser pulses is not strictly fixed due to the delays imposed upon these pulses, these fluctuations are insignificant with regard to the overall rate so that the average firing frequency remains unchanged. This keeps the laser cavity temperature stable so that a constant laser pulse energy and beam profile is maintained.

The smallest possible time step δ for the used microprocessor is $1 \mu\text{s}$, which, as a result, is the temporal resolution of the setup. Nyquist's criterion demands a sampling frequency of twice the frequency of the signal; hence the theoretical upper frequency limit is 500 kHz. However, in order to compute the amplitude and phase of a sine-shaped vibration with an acceptable reliability, experience teaches that the minimal number of phase steps is at least 4, hence the actual upper frequency limit for the setup is 250 kHz. This is merely limited by the trigger electronics and could be extended if needed.

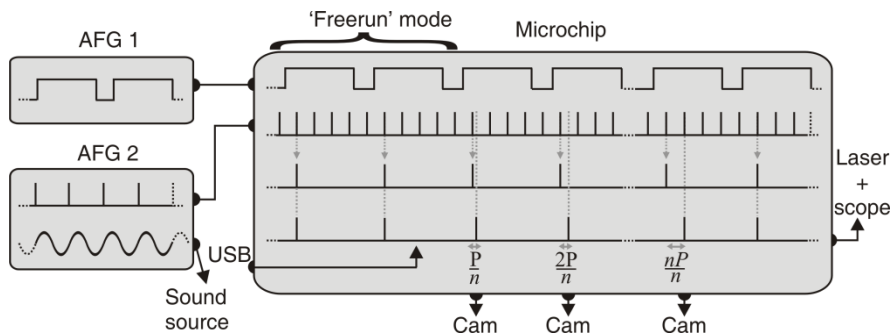


Figure 3: Close-up of the trigger sequence inside the microchip. The details are discussed in section 2.2.2.

2.2.3 Acoustic aspects: the acoustic stimulation element and sound phase measurement

For measurements using acoustic excitation, an acoustic stimulation element (ASE) was constructed and placed in front of the object (figure 2). The ASE is a fixed rigid tube with at one end an opening for the studied object and at the other end an oblique window. This window prevents the acoustic signal from escaping from this side, while allowing the laser beam to enter the element without producing disturbing reflections into the optical path thanks to its obliqueness.

The wall of the ASE contains two openings, one to provide an entrance for the acoustic stimulation and one for a probe tube microphone (Bruel & Kjaer 4182), of which the tip is placed at a distance of 5 mm away from the object. This probe microphone monitors the magnitude and phase of the acoustic stimulus so that the magnitude and phase of the object motion relative to the sound can be obtained. If we know the sound phase at the probe tip $\phi_{s,t}$, the sound phase at the object $\phi_{s,o}$ is equal to:

$$\phi_{s,o} = \phi_{s,t} + 2\pi \frac{5 \text{ mm}}{\lambda_s}, \quad (4)$$

with λ_s the sound wavelength, i.e. $\lambda_s = \frac{c}{f}$, with $c = 343$ m/s the speed of sound at room temperature and f the sound frequency. Equation (4) accounts for the phase delay of $2\pi \frac{d}{\lambda_s}$ for a sound wave with wavelength λ_s that travels a distance of $d = 5$ mm. The phase of the outgoing signal from the microphone controller $\phi_{s,OUT}$ is given by:

$$\phi_{s,OUT} = \phi_{s,t} + 2\pi \frac{l_t}{\lambda_s} + \phi_{el}, \quad (5)$$

with l_t the length of the tube, i.e. the distance of the probe tip to the microphone diaphragm and ϕ_{el} a phase difference due to electronic delays. The second term of the right hand expression in equation (5) is similar to the last term in equation (3). The last term accounts for additional phase delays imposed by the microphone preamplifier and controller (originating from frequency cut-off filters). Data for this phase delay are provided by the manufacturer's manual (Bruel and Kjaer 1990). Combining equations 4 and 5, the sound phase at the object can be determined from the knowledge of the phase of the microphone signal and the technical parameters of the microphone, provided by the manufacturer (Bruel & Kjaer). This signal is compared to the pulses that trigger the laser flash tube (the second output of the microprocessor in figure 2) on an oscilloscope. The actual light pulse is fired 4 to 5 ns after the pulse that is sent to the laser flash tube, which is a negligible time delay at all frequencies. In this way, we know the exact acoustic stimulus phase for every laser pulse and thus for every recorded hologram. Combined with the displacement results from stroboscopic holography, we are able to extract the object's full-field transfer function, defined as the complex vibration wave at every object point divided by the complex stimulus wave.

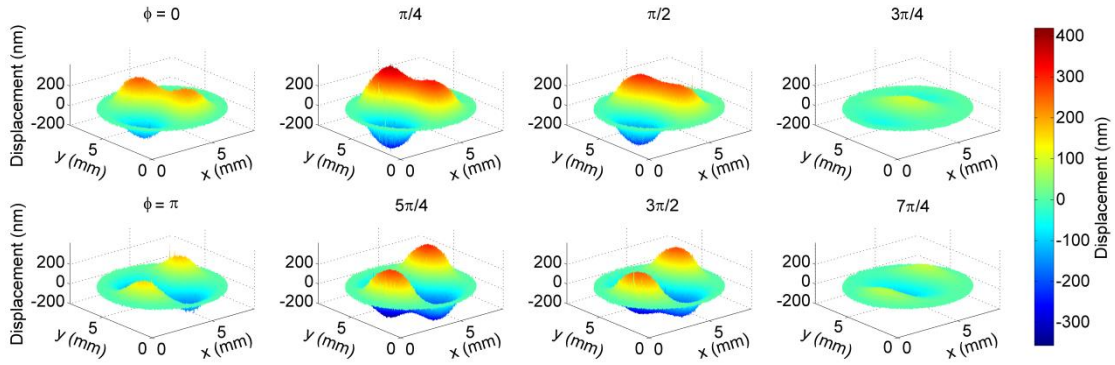


Figure 4: Displacement maps of a stretched rubber membrane acoustically stimulated at a frequency of 3805.5 Hz and a sound pressure of 100 dB SPL. The applied stroboscopic illumination is equivalent to figure 1.

3. Results

3.1 Vibration of a circular membrane

We present results on a stretched circular rubber membrane (diameter 8 mm, diffuse), excited acoustically at a broad frequency range (5 - 16752 Hz, covering more than 11 octaves), demonstrating the wide applicability of the technique. For this recording, the distance between the CCD target and the object was equal to 160 mm. The measurements were made using the acoustical stimulation element (ASE), as described in section 2.2.3, which provided controllable acoustic stimulation and monitoring. Figure 4 shows eight displacement maps of the membrane, excited at 3805.5 Hz with a SPL of 100 dB. The phase steps between each two consecutive maps are equal to $\pi/4$, i.e. $1/8^{\text{th}}$ of a period in terms of time, so that the pulses are distributed evenly inside the vibration period and this recording is consistent with the illumination in Figure 1.

In order to extract full field magnitude and phase information of the membrane's transfer function, we calculated the complex *FFT*-spectrum of the temporal displacement for every object point and extract the magnitude and phase of the principal component, i.e. the component that oscillates with the acoustic stimulus frequency. This component is generally much larger than other harmonics, which means that the motion is undistorted. The result of this full field *FFT* analysis is presented in figure 5 (left: magnitude map; right: phase map). The phase map in figure 5 (right)

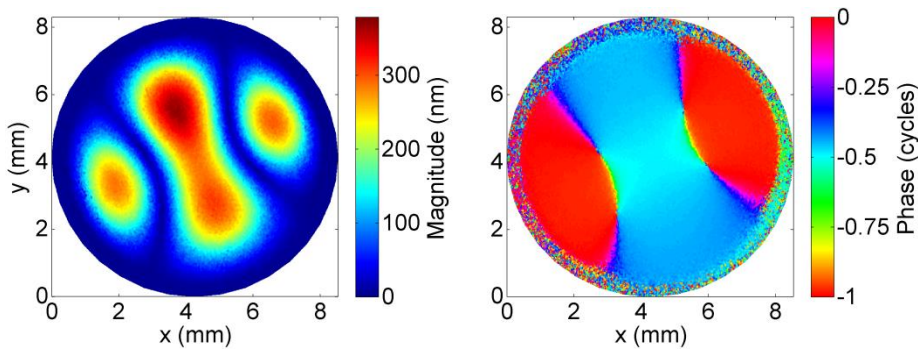


Figure 5: Full-field transfer function magnitude (left) and phase (right) maps of a stretched rubber membrane acoustically stimulated at a frequency of 3805.5 Hz and a sound pressure of 100 dB SPL. These figures originate from the same measurement data as figure 4.

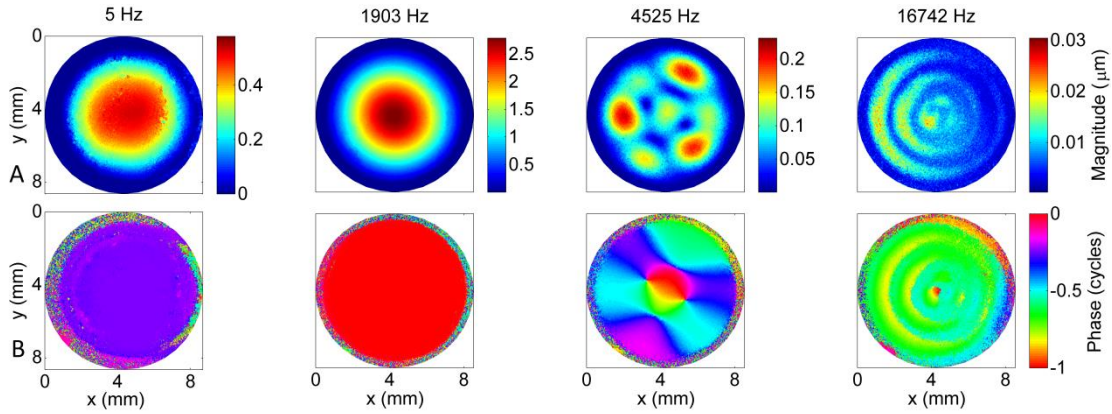


Figure 6: A. Magnitude maps and B. phase map of a vibrating membrane at different frequencies, covering the entire measurement range for our setup and this sample. The applied sound pressure values are 90 dB SPL for 5 Hz, 95 dB SPL for 1.9 kHz, 100 dB SPL for 4.5 kHz and 95 dB SPL for 16.7 kHz.

presents the phase of the object relative to the acoustic stimulus phase: a value of -0.25 cycles means that the object's vibration is delayed by a time of 0.25 times the period in relation to the stimulus. One clearly sees four local maxima in figure 5 (left), while continuous phase transitions are noticed over the entire membrane in figure 5 (right), indicating a non-modal pattern that is not predicted by a theoretical circular clamped elastic membrane (Fletcher 1992).

In figure 6, the magnitude (6A) and phase maps (6B) of four more vibrational patterns are presented with stimulation frequencies ranging from 5 Hz to 16.7 kHz. This shows that the developed setup produces acceptable to very good results for a frequency range of more than 11 octaves for this particular sample. At 5 Hz, the membrane is not exactly in phase with its stimulus, which could be due to viscoelastic effects of the material. At frequencies close to but below its resonance frequency (cfr. 1903 Hz in figure 6), the membrane moves exactly in phase with the sound stimulus.

3.2 Duration of the measurements

The optimal working frequency of the pulsed laser is 10 Hz, so the time needed to record n vibration holograms is n times 100ms. A measurement of vibration holograms at 8 phase steps thus takes 0.8 s plus the additional time needed to record a reference rest hologram which is around 1 s. The recording of 100 vibration holograms plus reference frame takes 11 s.

A full spectrum measurement from 25 Hz to 25600 Hz at 4 frequency steps per octave, i.e. 41 frequencies, at 8 vibration holograms plus 1 reference frame per frequency takes less than three minutes.

3.3 Evaluation of the technique: accuracy and repeatability

3.3.1 Accuracy

In order to evaluate the reliability of the technique, two test measurements were carried out. The first test evaluated the accuracy of the technique for measuring static deformations by imposing several known static displacements on the object. Holograms

of a surface are recorded before and after the deformation, and the full-field displacement is calculated from these two holograms. The deformation is realized by indenting it from the reverse side using a metal pin that is connected to a calibrated Piezo actuator. The used surface was a stretched rubber membrane. Figure 7 shows the result of this test measurement for applied indentations of 10nm, 500nm and 3 μm , covering the entire measurement range of the setup with this object. The smallest and largest deformations are at the limits of the technique's measurement range, so some challenges are to be expected.

A statistical analysis of the data is presented in Table 1. To obtain this numbers, data was taken from pixels that cover the indented surface of the object. The tip of the pin has a diameter of 1,3 mm and the pixel dimension is 10 μm and 12 μm in x - and y -directions, so data within a circle with radius 50 pixels around the center of the indented area was extracted. The statistical average and standard deviation (SD) are shown in Table 1, as well as the relative SD (i.e. the SD divided by the average). The standard deviation was calculated by:

$$\sigma_z = \sqrt{\frac{\sum_i (z_i - \langle z \rangle)^2}{N}}, \quad (6)$$

with N the number of selected pixels. The motivation for this form is the assumption that the chosen dataset to be the entire population (opposed to a partial population, in which case the denominator should be $\sqrt{N-1}$). The correspondence between the applied and measured deformation is a measure for accuracy, whereas the SD and relative SD can be interpreted as measures for the precision of the technique. While the SD increases with increasing deformation, the relative SD decreases.

In the case of smallest indentation, the maximal displacement at a single data point is 13.6 nm, which is larger than the applied 10 nm. However, when averaging a circle with a radius of 50 pixels at the location where the indentation was applied, this value dropped to 10.1 nm, indicating that the error of 3.5 nm in one of the pixels is due to measurement noise. Nevertheless, thanks to the excellent spatial resolution, the indentation peak is unmistakably detectable. Displacement values lower than 0 near the edge of the membrane are probably caused by very small static motions between the recording of the reference frame and the deformation frame.

Accuracy measurement results

Indentation (nm)	$\langle z \rangle$ (nm)	σ_z (nm)	σ_{rel}
10	10,1	1,0	9,9%
500	474,8	6,9	1,5%
3000	2848	37	1,3%

Table 1: Overview of accuracy measurement results. The first column presents the applied indentation using a Piezo actuator; the second column lists the average measured deformation in a circle with a diameter equal to the used indentation pin; the third and fourth column provide the standard deviation and relative standard deviation on this data.

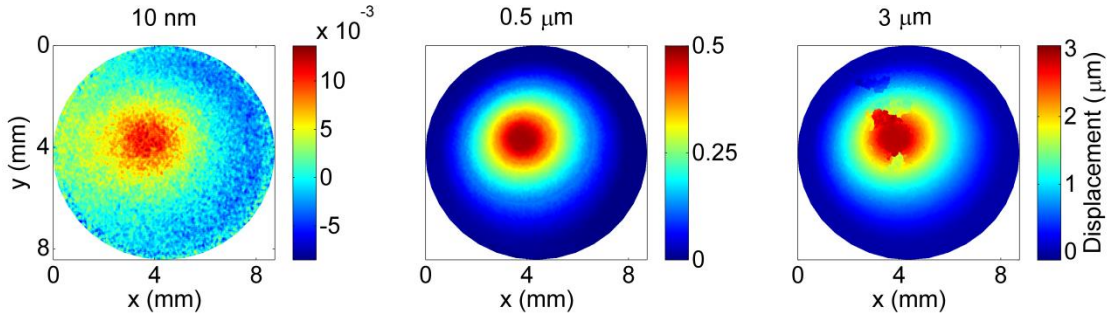


Figure 7: Accuracy test measurements of static deformations at the edges and in the middle of the measurement range for our setup and the chosen demonstration sample. The displacements were applied by a metal pin connected to a piezo transducer. Chosen indentation values are 10 nm, 0.5 μm and 3 μm .

As can be seen in Figure 7, the displacement map for the largest indentation (3 μm) shows some issues that are the result of phase unwrapping errors. In these areas, the high density of $\pi/2$ phase jumps in combination with a possible slightly lower reflectivity in these areas of the surface, cause wrongly detected $\pi/2$ -jumps and thus erroneous unwrapping results.

At the largest indentation values, the measured deformation is significantly lower than the applied indentation (see Table 1). This is probably caused by compression of the rubber membrane due to the pressure applied by the indentation pin, rather than a systematic error in the technique.

3.3.2 Repeatability

The second test evaluated the repeatability of the setup through a repeated full-spectrum analysis of a membrane using the same input stimuli at the same frequencies without changing anything of the setup in between measurements and with an interval of 3 minutes between measurements. The results of the repeatability measurements are presented in figures 8 (magnitude) and 9 (phase), where the frequency-dependent transfer function of the center point of the membrane is shown. These data were extracted from a single data point and neither smoothing nor averaging has been applied to reduce noise effects.

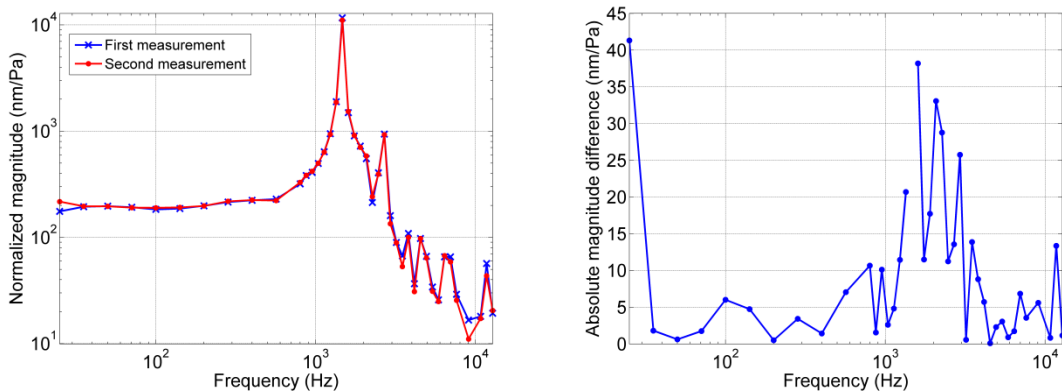


Figure 8: Left: Transfer function magnitude results from two full-spectrum repeatability tests. Results are extracted from the center point a vibrating rubber membrane. In between measurements, an interval of 3 minutes was left. Right: Absolute magnitude difference between the repeated measurements. Only close to the resonance peak (1.2 – 2 kHz) and at quasi-static frequencies, this difference is significant. In both these regions, the differences are due to the sample and the stimulating device rather than the technique itself, as discussed in section 3.3.

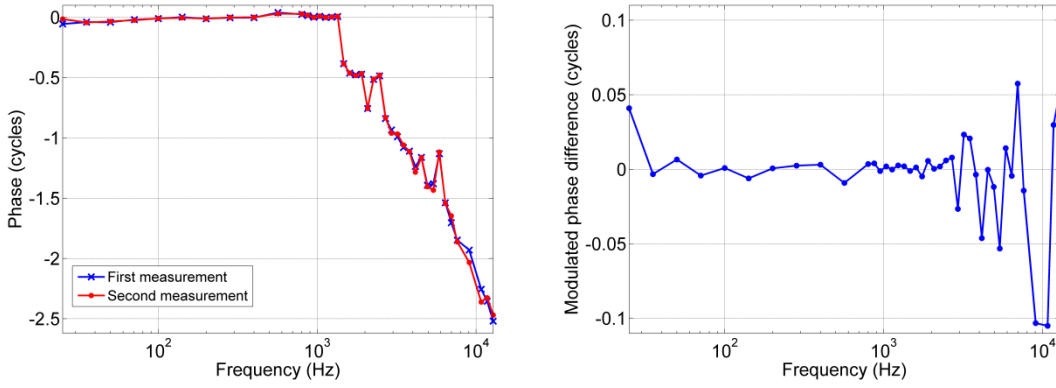


Figure 9: Left: Transfer function phase results from the two full-spectrum repeatability tests. These figures originate from the same data as figure 8. Right: Modulated phase difference between the repeated measurements. The most distinct differences are found at the highest frequencies, where small errors in time measurements can lead to significant phase differences.

For the sake of consistent evaluation, the data of both the magnitude and phase are normalized to the incident sound pressure. 43 frequencies are measured: 2 logarithmically spaced points per octave in the range 25 – 800 Hz and 8 per octave in the range 0.8 – 12.8 kHz. The reason for this uneven distribution is the more complex and quickly changing behavior on the higher frequencies. Unreliable measurements at 8.30 kHz and 9.87 kHz were removed from the dataset, since the used speaker was not able to produce acceptable sound signals at these frequencies.

The calculated intra-class correlation (ICC) coefficients of these repeated datasets were 99,86% for the magnitude and the 99,92%, indicating a very good repeatability (McGraw and Wong 1996).

The absolute magnitude difference in figure 8 (right) is defined as:

$$m_{diff} = |m_2 - m_1|, \quad (7)$$

with m_1 and m_2 being the frequency dependent magnitude from the first and second measurement, respectively. Overall, the average absolute magnitude difference is 8,7 nm/Pa. At most frequencies lower than 1200 Hz and higher than 2000 Hz, this value is well below 10nm. As can be expected, difference values are higher in areas where the transfer function has large values and steep tangents, i.e. close to the sample's resonance frequency. One data point very close the resonance frequency (at 1467 Hz) was considered as unrepresentative and was removed from the figure as in this very narrow but sensitive area the repeatability of the measurement is far more dependent on the sample than on the technique itself. Indeed, the sample, an undamped vibrating membrane, features a very sharp and high resonance peak, so that a tiny shift in resonance frequency causes the measured magnitude at a frequency close to this peak to change strongly compared to other frequencies. At quasi-static frequencies, the larger difference is explained by difficulties from the speaker to produce a harmonic acoustic signal with a sufficient pressure level at this frequency. Therefore, a lower sound pressure level is applied (90 dB instead of 100 dB or more like at most other frequencies), resulting in a smaller motion range and a lower signal-to-noise ratio. This induces a larger random relative error and thus a larger difference between subsequent

measurements. Furthermore, the measurement result at this frequency is possibly influenced by viscoelastic effects of the sample as well.

The modulated phase difference in figure 9 (right) is defined as:

$$p_{diff} = \begin{cases} \text{mod}(p_2 - p_1, 1) & \text{if } < 0.5 \\ \text{mod}(p_2 - p_1, 1) - 1 & \text{if } > 0.5' \end{cases} \quad (8)$$

with p_1 and p_2 being the frequency dependent phase from the first and second measurement, respectively. By applying this modulation, all values lie between -0.5 and 0.5 cycles. Overall, the average of the absolute value of the phase difference is 0,017 cycles. The absolute value of the modulated phase difference is well below 0.05 cycles for most frequencies below 7 kHz and is more variable for values above 7 kHz. At these high frequencies, however, very small errors in time measurement can lead to considerable differences in phase. A preferred sign for the phase difference is observed in none of the frequency ranges, so the errors appear to be random rather than systematic.

4. Discussion

4.1 Measurement range

The measurement range is difficult to determine since it is dependent on a large number of factors. On our demonstration sample, motion amplitude needed to have a magnitude of at least 5 nm in order to be distinguishable from the measurement noise. Since magnitude is a function of frequency and this response function can differ between different samples, the frequency range of the technique can be different for other samples. Furthermore, the level of noise is also variable, depending on the sample's reflectivity. The maximal measurable displacement is dependent on the density of 2π -jumps on the object surface. If these jumps are too close to each other, unwrapping algorithms are incapable of extracting the unwrapped phase map such as demonstrated in figure 7 (right). Thus, the upper measurement limit is dependent on the maximal displacement, the number of pixels covering the studied surface and the complexity of the vibration pattern, which determines the steepness of the shape of the displacement maps. The maximal magnitude that was measurable on our demonstration sample was around 5 μm (sample covered 670 x 822 pixels). Furthermore, in order to study single harmonically isolated motions, the setup range is limited by the range of the chosen excitation device in which one can be certain of undistorted sine-wave stimulus signals.

The spatial resolution of the setup is also dependent on different parameters and is given by (Kreis 2005):

$$\Delta x = \frac{d\lambda}{N\Delta\xi}, \quad (9)$$

with d being the chosen reconstruction distance, λ the laser wavelength, N the number of CCD pixels and $\Delta\xi$ the CCD center-to-center pixel distance. In our setup, this resulted in a lateral spatial resolution of 10 μm in x -direction and 12 μm in y -direction.

4.2 Comparison to other techniques

The advantage of the presented time-resolved full field imaging technique over time-average holography (Powell and Stetson 1965) and its digital variant is obvious, since time-averaging does not provide any time-resolved information at all. Therefore, vibrations studied with time-average holography can be mistakenly identified as purely modal with strict in- and out-of-phase regions and nodal lines, while in reality there could be significant continuous phase gradients over the surface, such as seen in figures 5 (right) and 6B (at frequencies above 3000 Hz). Stroboscopic holography however requires a longer and more complicated recording procedure.

Another important advantage of the presented technique is the capability of single-shot full-field measurement with an excellent spatial resolution without the need for scanning, as opposed to laser Doppler vibrometry (LDV) based approaches (Lewin, Mohr, and Selbach 1990).

A disadvantage is its sensitivity to (quasi-)static motions in between recordings. On the other hand, methods that measure velocity instead of displacements, such as scanning LDV, are by design insensitive to uncontrolled (quasi-)static motions.

4.3 Comparison to similar setups

Stroboscopic digital holography is not a new technique in itself. In 1986, Hariharan and Oreb published a hybrid setup that utilized a holocamera to record double-exposure pulsed analogue holograms on a television camera, thereby not being true digital holography (Hariharan and Oreb 1986). More recently, stroboscopic holography was truly digitized when phase-shifted double-exposure holograms were recorded on a digital CCD camera for subsequent reconstruction (Furlong et al. 2009; Hernandez-Montes et al. 2009). In other approaches, the laser pulses were not only timed at two opposite phases within the vibration period, but spread out to different vibration phases (Pedrini, Osten, and Gusev 2006; Trillo et al. 2009; Cheng et al. 2010), such as in figure 1 from this paper. The approaches chosen in (Pedrini, Osten, and Gusev 2006) and (Trillo et al. 2009) are based on a high-power continuous laser (~ 10 W) and high frame rate recordings (within-period acquisition) and are both aimed for industrial applications at < 1 kHz frequencies. Although very promising setups, no follow-up studies have been published. The setups feature camera frame rates of 4.000 – 10.000 fps, posing an intrinsic limitation of around 1-2 kHz on the highest frequency that can be measured by the setups. Provided that a very expensive ultra-high frame rate camera of ~ 500.000 fps is used, this limit could be increased to ~ 100 kHz. However, provided that the motion is periodic, the setup presented in the current paper is able to measure up to 250 kHz using a low frame rate camera. As discussed in section 4.1 even higher frequencies are achievable when using further optimized electronics, which is not expensive at all in comparison to ultra-high frame rate cameras. Furthermore, as the camera frame rate is no limiting factor in our setup, the CCD target resolution can be allowed to be much higher (2452x2054), compared to 256x256 (Pedrini, Osten, and Gusev 2006) and 856x848 (Trillo et al. 2009) in the mentioned papers. The advantages of more available pixels include a better spatial resolution and a lower limit on the allowed distance between the camera and the object.

The approach chosen by (Cheng et al. 2010) is the one closest to the currently presented setup. In that setup, however, a continuous laser was strobed using an acousto-optic modulator, resulting in lower energy pulses compared to our setup, in which a high-energy pulsed laser has been introduced. In order to collect a sufficient amount of light on the CCD using the lower power pulses, longer pulse lengths are needed (10 % of the vibration period) and a number of these pulses need to be integrated, causing three disadvantages compared to our setup. Firstly, since the illumination covers 10% of the vibration period, different positions in time of the objects will contribute to the recorded hologram, resulting in a loss of resolution. Secondly, since the pulse length increases for decreasing frequency, stability problems arise in the low-frequency range, resulting in a low-frequency limit of 200 Hz in the published results. Thirdly, the capability of recording single-shot holograms with an ultra-short single laser pulse enables us to extend the technique to measurement of extremely fast transient phenomena with a sub-microsecond temporal resolution, as discussed in the next section. These resolutions are not achievable when using a strobed continuous wave laser. Furthermore, the mentioned setup does not record a reference hologram in rest state, but rather computes deformations between every subsequent vibration hologram (at stimulus phases $\pi/4$, $\pi/2$, $3\pi/4$...) and the vibration hologram at stimulus phase zero. This does not allow the determination of absolute displacement maps, since the surface's shape at stimulus phase zero is not always equal to its shape in rest, certainly at higher frequencies.

4.4 Applications and future development

Our lab uses the presented technique to study the motion of the eardrum of humans, other mammals and avian species. Acquiring full-field vibration response information of these membranes across both quasi-static and acoustic frequencies is of major interest in a better understanding of the characteristics and the role of the eardrum. The results are used as validation data for finite element models with highly realistic geometries, so that we can construct a true-to-nature computer model of the entire human middle ear. Steps in this direction have been made already (De Greef et al. 2014; Aernouts, Aerts, and Dirckx 2012) and further developments in this research line will be published in the future.

The technique can however be used in many other fields than biomechanics, basically in any field where full-field vibration information in a frequency range from 1 Hz to 250 kHz could be valuable.

In the future, the setup will be adapted to measure very rapid transient motions. Such measurements are important to characterize viscoelastic behavior of materials, or to study propagation of traveling waves. Since the laser pulses have a length of 8 ns and one pulse is sufficient to record a hologram, very rapid transient motions can be visualized with a temporal resolution of 1 μ s, which currently is the smallest time step on our microchip's program. With further optimized trigger electronics, the setup could be able to measure transient motions with a sub-microsecond temporal resolution. Note that the transient phenomenon needs to be reproducible, as the different holograms cannot be recorded during a single event.

5. Conclusion

In this paper, a new setup for stroboscopic digital holography, incorporating a high-energy pulsed laser and advanced trigger electronics, was described and presented. The basic concepts of digital and stroboscopic digital holography, as well as the technical details, including optical, electric and acoustic aspects, were covered. Results of measurements on a vibrating rubber membrane are shown in section 3, for frequencies ranging from 5 Hz to 16.7 kHz. This range is limited by the demonstration object and the stimulation device (i.e. in our case an acoustic speaker) rather than the technique itself. It needs to be noted that the possible range of the technique with the current components extends to 250 kHz. Furthermore, measurements are very quick, as shown in section 3.

Two tests were performed to make an assessment of the accuracy and repeatability of the technique: known static displacements were measured (for accuracy and precision) and a full-spectrum series of vibration measurement was tested for its repeatability. The accuracy tests revealed that the measured displacements are in good accordance with the applied indentations, provided that material compression was taken into account. The standard deviation of the technique increases from 1,0 nm at 10 nm indentation to 37 nm at 3 μm indentation, with the relative standard deviation decreasing from 9,9 % to 1,3% in the same range. The repeatability tests showed intra-class correlation coefficients of 99,86% and 99,92% for the magnitude and phase, respectively. The average absolute magnitude and phase difference at a single data point between subsequent measurement of the same phenomenon was 8,7 nm/Pa and 0,017 cycles, respectively, averaged over all frequencies.

The measurement range of the technique was discussed in depth and shown to be dependent on several factors such as camera resolution, object dimensions, light reflectivity and limits of the stimulation device. The technique was qualitatively compared to other techniques and setups that are similar to ours. Finally, possible applications, such as providing validation data for finite element models, and future ambitions, such as adapting the setup for measuring extremely fast transient phenomena, were addressed.

Acknowledgement

This project was funded by the Research Foundation Flanders (FWO) and the University of Antwerp. We thanks W. Deblauwe and F. Wiese for their technical support

References

- Aernouts, Jef, Johan R M Aerts, and Joris J J Dirckx. 2012. Mechanical Properties of Human Tympanic Membrane in the Quasi-Static Regime from in Situ Point Indentation Measurements. *Hearing Research* 290(1-2). Elsevier B.V. 45–54.
- Bruel & Kjaer. 1990. Probe Microphone Type 4182 User manual
- Cheng, Jeffrey Tao, Antti A Aarnisalo, Ellery Harrington, Maria del Socorro Hernandez-Montes, Cosme Furlong, Saamil N Merchant, and John J Rosowski. 2010. Motion of the Surface of the Human Tympanic Membrane Measured with Stroboscopic Holography. *Hearing Research* 263(1-2). Elsevier B.V. 66–77.
- De Greef, Daniël, Jef Aernouts, Johan Aerts, Jeffrey Tao Cheng, Rachel Horwitz, John J. Rosowski, and Joris J.J. Dirckx. 2014. Viscoelastic Properties of the Human Tympanic Membrane Studied with Stroboscopic Holography and Finite Element Modeling. *Hearing Research* 312(March). Elsevier B.V: 69–80.
- De Greef, Daniël, and Joris J J Dirckx. 2014. A Synchronized Stroboscopic Holography Setup for Traveling Wave Analysis on Biomechanical Structures. In *Fringe 2013: 7th International Workshop on Advanced Optical Imaging and Metrology*, edited by Wolfgang Osten, 433–38. Berlin, Heidelberg: Springer Berlin Heidelberg.
- De Greef, Daniël, and Joris J. J. Dirckx. 2012. Single-Shot Digital Holographic Interferometry Using a High Power Pulsed Laser for Full Field Measurement of Traveling Waves. In *AIP Conference Proceedings* 1457, 1457:444–50.
- Fletcher, Neville H. 1992. *Acoustic Systems in Biology*. New York: Oxford University Press.
- Furlong, Cosme, John J Rosowski, Nesim Hulli, and Michael E Ravicz. 2009. Preliminary Analyses of Tympanic-Membrane Motion from Holographic Measurements. *Strain* 45(3): 301–9.
- Hariharan, P., and B.F. Oreb. 1986. Stroboscopic Holographic Interferometry: Application of Digital Techniques. *Optics Communications* 59(2): 83–86.
- Hernandez-Montes, Maria del Socorro, Cosme Furlong, John J Rosowski, Nesim Hulli, Ellery Harrington, Jeffrey Tao Cheng, Michael E Ravicz, and Fernando Mendoza Santoyo. 2009. Optoelectronic Holographic Oscope for Measurement of Nano-Displacements in Tympanic Membranes. *Journal of Biomedical Optics* 14(3): 034023.
- Herráez, Miguel Arevallilo, David R Burton, Michael J Lalor, and Munther a Gdeisat. 2002. Fast Two-Dimensional Phase-Unwrapping Algorithm Based on Sorting by Reliability Following a Noncontinuous Path. *Applied Optics* 41(35): 7437–44.
- Kreis, Thomas. 2005. *Handbook of Holographic Interferometry*. Weinheim, FRG: Wiley-VCH Verlag GmbH & Co. KGaA.

- Lewin, A., F. Mohr, and H. Selbach. 1990. Heterodyn-Interferometer Zur Vibrationsanalyse / Heterodyne Interferometers for Vibration Analysis. *Tm - Technisches Messen* 57(JG): 335–45.
- McGraw, Kenneth O., and S. P. Wong. 1996. Forming Inferences about Some Intraclass Correlation Coefficients. *Psychological Methods* 1(1): 30–46.
- Pedrini, Giancarlo, Wolfgang Osten, and Mikhail E Gusev. 2006. High-Speed Digital Holographic Interferometry for Vibration Measurement. *Applied Optics* 45(15): 3456–62.
- Powell, Robert L., and Karl A. Stetson. 1965. Interferometric Vibration Analysis by Wavefront Reconstruction. *Journal of the Optical Society of America* 55(12): 1593–97.
- Rosowski, John J, Jeffrey Tao Cheng, Michael E Ravicz, Nesim Hulli, Maria del Socorro Hernandez-Montes, and Ellery Harrington. 2009. Computer-Assisted Time-Averaged Holograms of the Motion of the Surface of the Mammalian Tympanic Membrane with Sound Stimuli of 0.4-25 kHz. *Hearing Research* 253(1-2). Elsevier B.V. 83–96.
- Trillo, Cristina, Angel F Doval, Fernando Mendoza-Santoyo, Carlos Pérez-López, Manuel de la Torre-Ibarra, and J Luis Deán. 2009. Multimode Vibration Analysis with High-Speed TV Holography and a Spatiotemporal 3D Fourier Transform Method. *Optics Express* 17(20): 18014–25.
- Yamaguchi, Ichirou, and Tong Zhang. 1997. Phase-Shifting Digital Holography. *Optics Letters* 22(16): 1268–70.